Supporting Information

Selective methane electrosynthesis enabled by a hydrophobic carbon coated copper core-shell architecture

Xin Yu Zhang,‡[a] Wen Jing Li,‡[a] Xue Feng Wu,[a] Yuan Wei Liu,[a] Jiacheng Chen,[b] Minhui Zhu,[b] Hai Yang Yuan,*[a] Sheng Dai,[c] Hai Feng Wang,[d] Zheng Jiang,[e] Peng Fei Liu,*[a] and Hua Gui Yang*[a]

[a] Key Laboratory for Ultrafine Materials of Ministry of Education, Shanghai Engineering Research Center of Hierarchical Nanomaterials, School of Materials Science and Engineering, East China University of Science and Technology, 130 Meilong Road, Shanghai, 200237 (China)

[b] State Key Laboratory of Chemical Engineering, School of Chemical Engineering, East China University of Science and Technology, 130 Meilong Road, Shanghai 200237 (China)

[c] Key Laboratory for Advanced Materials and Feringa Nobel Prize Scientist Joint Research Center, Institute of Fine Chemicals, School of Chemistry and Molecular Engineering, East China University of Science and Technology, 130 Meilong Road, Shanghai, 200237 (China)

[d] Key Laboratory for Advanced Materials, Centre for Computational Chemistry and Research Institute of Industrial Catalysis, School of Chemistry and Molecular Engineering, East China University of Science and Technology, 130 Meilong Road, Shanghai, 200237 (China)

[e] Shanghai Synchrotron Radiation Facility, Shanghai Advanced Research Institute, Chinese Academy of Sciences, 239 Zhangheng Road, Shanghai, 201204 (China)

Experimental Section

Preparation of H-CuO_x@C-CTAB-1 electrodes

The sample ink was prepared by dispersing 5 mg H-CuO_x@C, 1 mg cetyltrimethylammonium bromide (CTAB), and 50 µL Nafion solution into 0.125 mL H_2O and 0.375 mL isopropanol followed by sonication for more than 30 min. 2.5 µL ink was dropped on GCE (with a diameter of 3 mm) and dried in the air for 2 times.

Preparation of H-CuO_x@C-CTAB-2 electrodes

The preparation method was the same as above except that the amount of CTAB was increased to 5 mg.

Characterizations

In-situ diffusion reflectance infrared Fourier transform spectra of H_2O adsorption were recorded using a Fourier transform infrared spectrometer (PerkinElmer, Frontier) with a mercury cadmium telluride (MCT-A) detector and an *in-situ* cell (modified Harrick Model HV-DR2). About 50 mg of catalyst was ground and placed into the sample holder. The sample was firstly heated at 60 °C for 30 min to remove moisture. Background spectra were then collected. Afterwards, moisture was introduced by flowing Ar through an H_2O bubbler (at room temperature) for 20 min, with the spectrum collected every minute. The infrared data were evaluated in KubelkaMunk units, which are linearly related to the absorber concentration in spectra.

Double-layer capacitance (C_{dl}) measurements

C_{dl} of catalysts were obtained by measuring cyclic voltammetry (CV) in the potential ranges between -0.2 and -0.1 V vs. RHE where no Faradaic process occurred with different scan rates (20, 30, 40, and 50 mV s^{-1}, respectively). The CV measurement was operated in the same H-type reactor and 0.1 M $KHCO_3$ was used as the electrolyte. By plotting the average current Δj ($\Delta j=(j_{anodic}-j_{cathodic})/2$ at -0.15 V vs. RHE) against the scan rate, C_{dl} value was given by the slope.

Multi-point averaging molecular dynamics (MPA-MD) method

In MPA-MD simulation, first, we performed the Ab initio molecular dynamics (AIMD) calculations of each intermediate state (*CO, *CHO, *COH, *OCCO) on Cu(111) and clean Cu(111) surface, in which different water quantities(3 H_2O, 4 H_2O, 5 H_2O, and 15 H_2O, respectively) were applied above the surface as an initial aqueous network at the liquid/solid interface. Only the Γ-point was used to sample the Brillouin zone. The simulation temperature was set to 300 K (experimental temperature) with a 1 fs movement for each step in the canonical (NVT) ensemble employing Nosé-Hoover thermostats. Nearly 10 ps MD simulations were performed, and all the simulations reach the equilibrium plateau after ~4 ps.

Then, we selected structures from the stabilized MD simulations (small fluctuation in energy after long simulations, ~ 4 ps), and further optimized them to obtain the total energy (E_{tot}) of each structure. For each intermediate, around 10 samples from the late part of each overall MD simulation were obtained. Considering that different solution structures of the water network affect E_{tot}, we deducted the contribution of the water solution in E_{tot} but still considered the solvation effect for each sample as follows:

(i) We calculate the total energy of the water solution (E_{H2O}) with exactly the same structure as in the optimized samples.

(ii) We deduct E_{H2O} from E_{tot} to obtain the solvation-included energy.

(iii) Finally, we average the obtained solvation-included energies of all the samples in each intermediate as the following formula: $\Delta E = \frac{1}{10}\sum_{10}^{i} (E_{\mathrm{tot}} - E_{\mathrm{H2O}})$.

Through the MPA-MD calculations, we can obtain the solvation-included reaction energies of all the samples at different water concentrations, which is closer to the realistic reaction situation. Thus, we can correctly evaluate the possibility of different elementary reaction pathways. The results from MPA-MD (Figure 1c) show that *CHO has the greatest advantage in the presence of low H_2O content compared with *CO, *COH, and *OCCO, i.e., *CO protonation to form CH_4 is more feasible as H_2O content is low on the Cu surface.

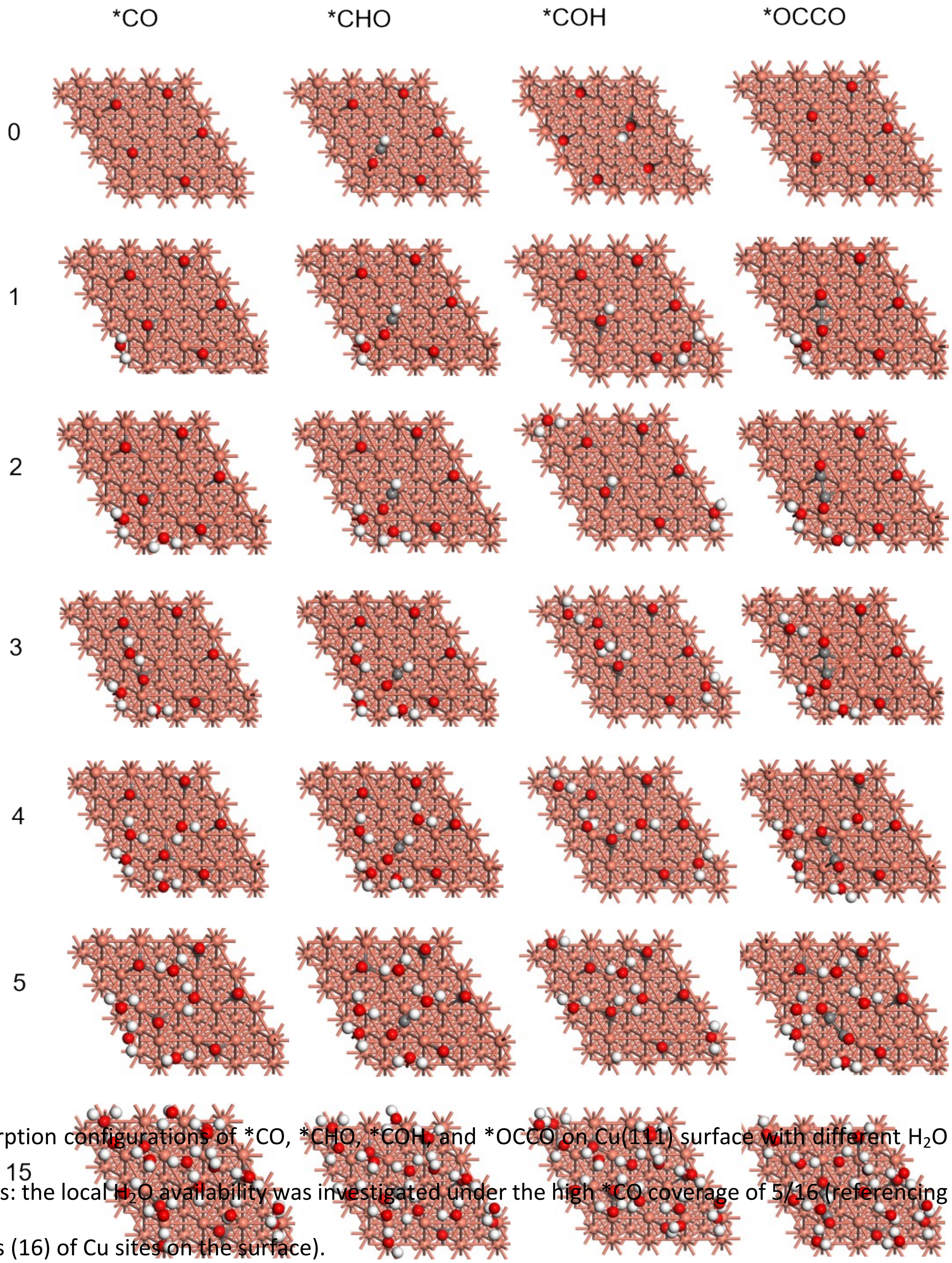

Figure S1. Adsorption configurations of *CO, *CHO, *COH, and *OCCO on Cu(111) surface with different H_2O quantities. Notes: the local H_2O availability was investigated under the high *CO coverage of 5/16 (referencing to the quantities (16) of Cu sites on the surface).

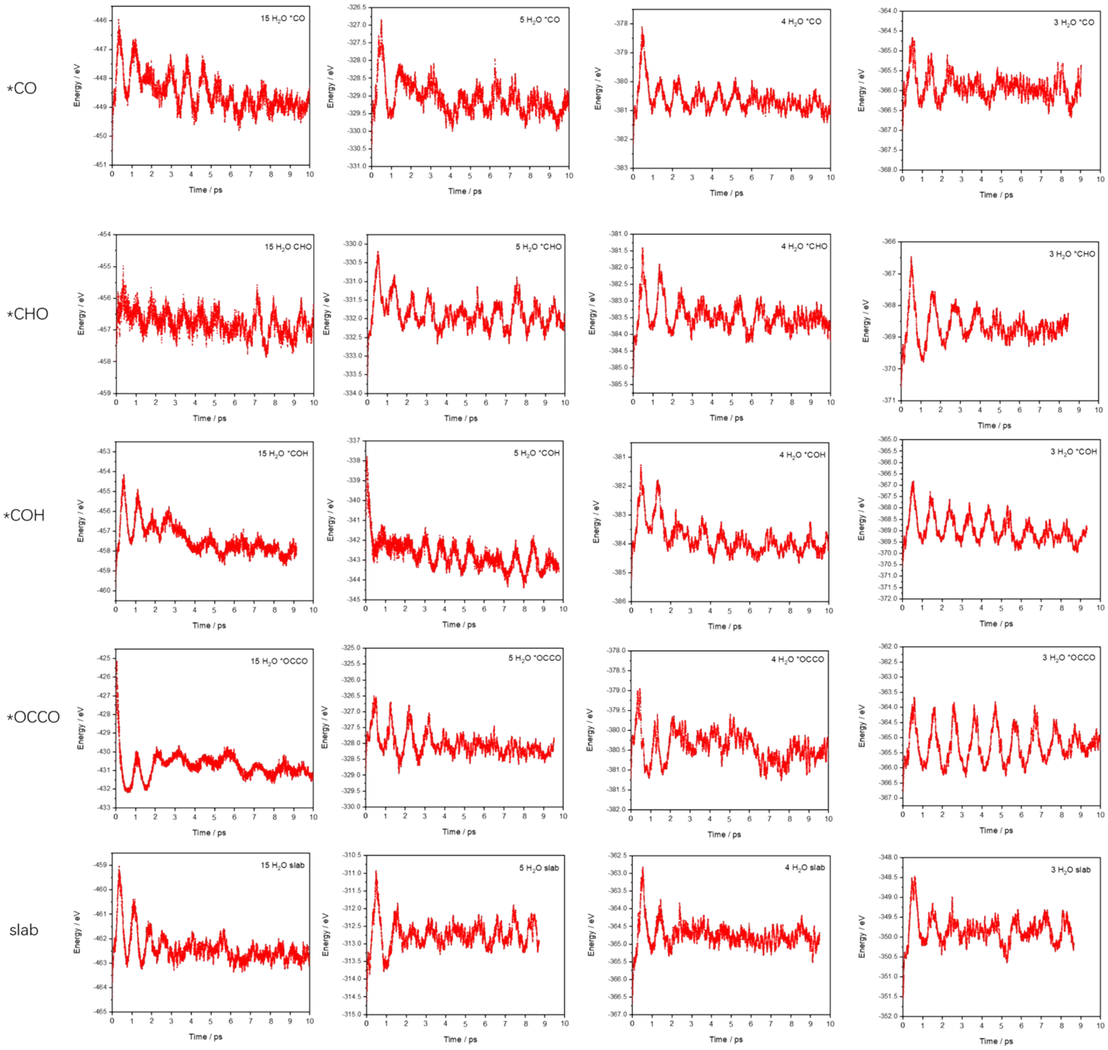

Figure S2. Energy profiles of MD simulations for water (15 H_2O, 5 H_2O, 4 H_2O, and 3 H_2O molecules)/Cu (111) for *CO, *CHO, *COH, *OCCO, and clean surface. MD simulations (about 10 ps) reached quasi-equilibrium after ~4 ps.

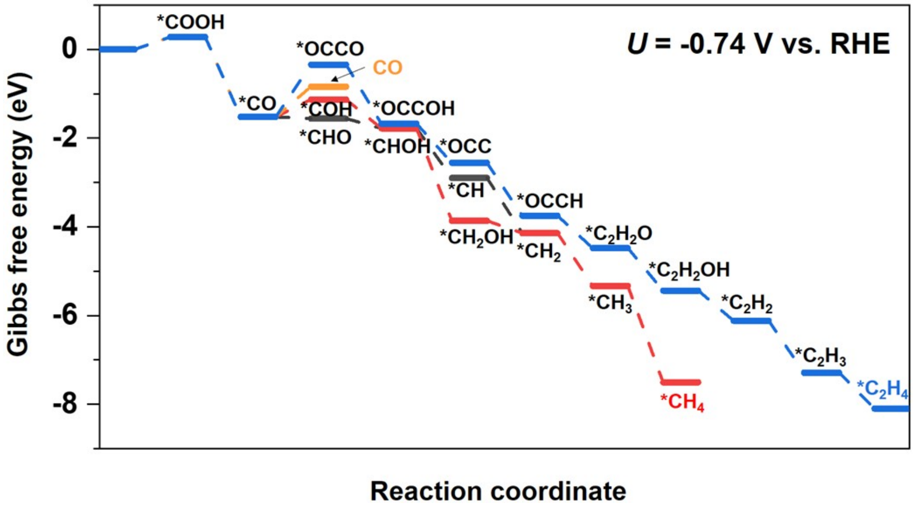

Figure S3. The whole free energy diagrams of CO, CH_4, and C_2H_4 formations with 2 H_2O molecules (*U* = -0.74 V vs. RHE).

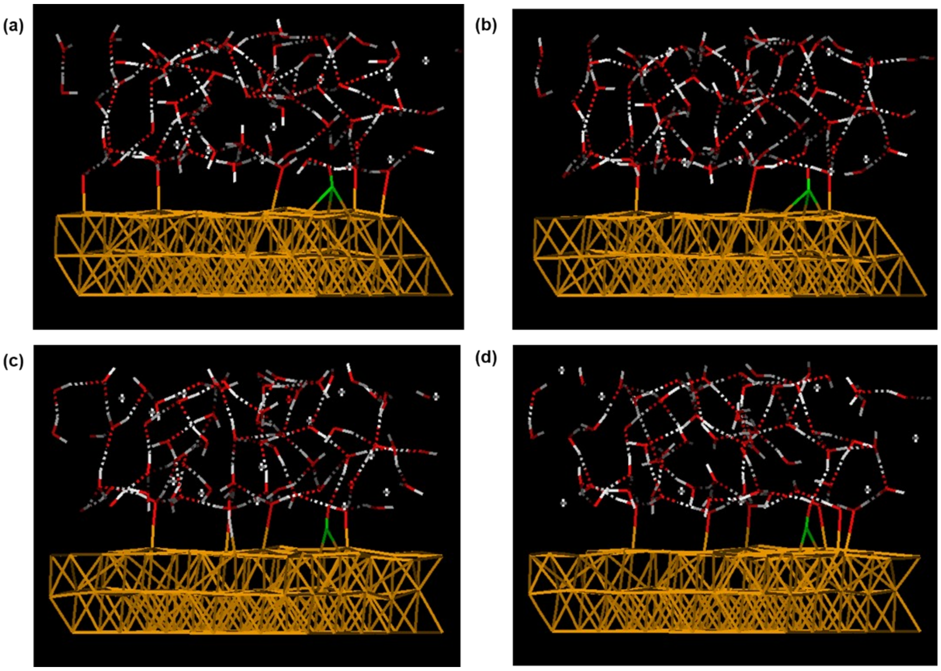

Figure S4. Schematic diagram from MD simulation for *CO transferring on Cu(111), (a-d) respect diagrams at 6.45 ps, 6.47 ps, 6.49 ps, and 6.51 ps of MD simulation, which indicates the steric squeezing of abundant water molecules on *CO. As H_2O content increases, it can be expected that H_2O molecules aggregate around *CO and even some H_2O molecules trend to adsorb on the Cu surface, and the steric squeezing from H_2O molecules could decrease the adsorption strength of CO on Cu(111) surface, leading to *CO on the hollow site transferring to the bridge or top site. Therefore, it can be expected that the steric squeezing from abundant H_2O molecules could decrease the desorption energy of CO on Cu(111). This gif was also uploaded as a supplementary file.

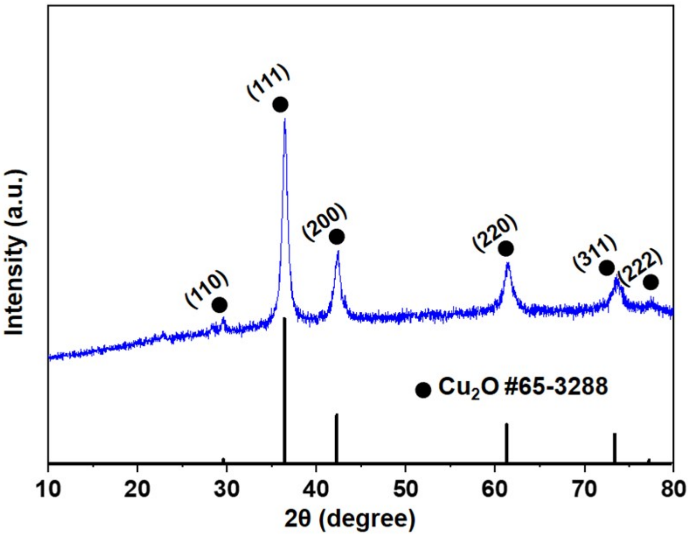

Figure S5. XRD pattern of W-CuO_x control sample, which indicates the crystalline phase of Cu_2O, without the metallic Cu species resulting from the lack of reductive agent.

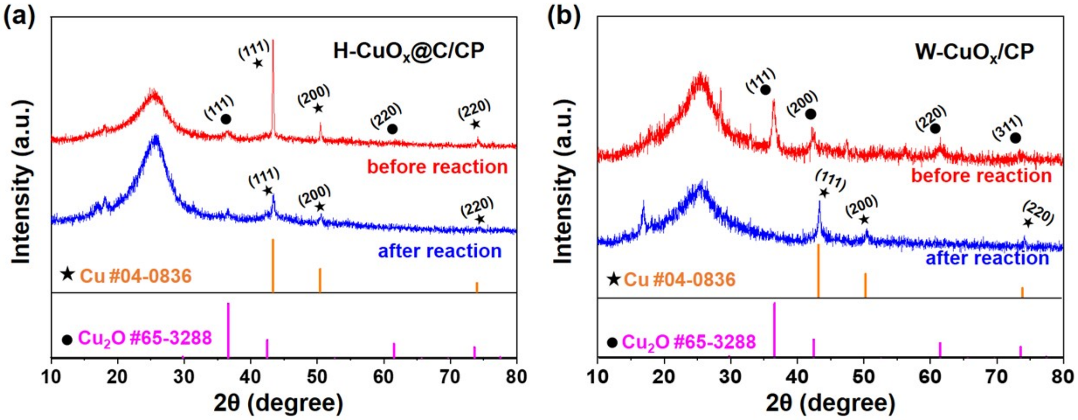

Figure S6. XRD pattern of (a) H-CuO$_x$@C and (b) W-CuO$_x$ on the carbon paper substrate before and after 2 hour's CO$_2$RR at the potential of -1.40 V vs. RHE, showing the Cu$_2$O phase has been reduced to metallic Cu during the test, and both of H-CuO$_x$@C and W-CuO$_x$ samples exhibit obvious Cu(111) diffraction peaks. Notes: the weak diffraction peak of Cu$_2$O after reaction might be attributed to the surface oxidation in the air.

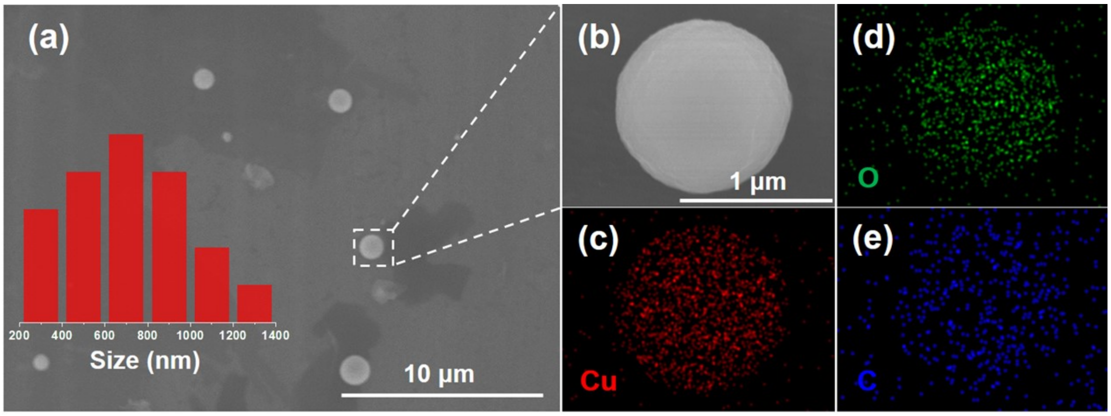

Figure S7. (a) SEM image of the as-synthesized H-CuO_x@C sample. Inset of (a): particle size distribution. (b) The typical SEM image of H-CuO_x@C particle and (c-e) corresponding elemental mapping images of (c) Cu, (d) O, and (e) C elements, respectively.

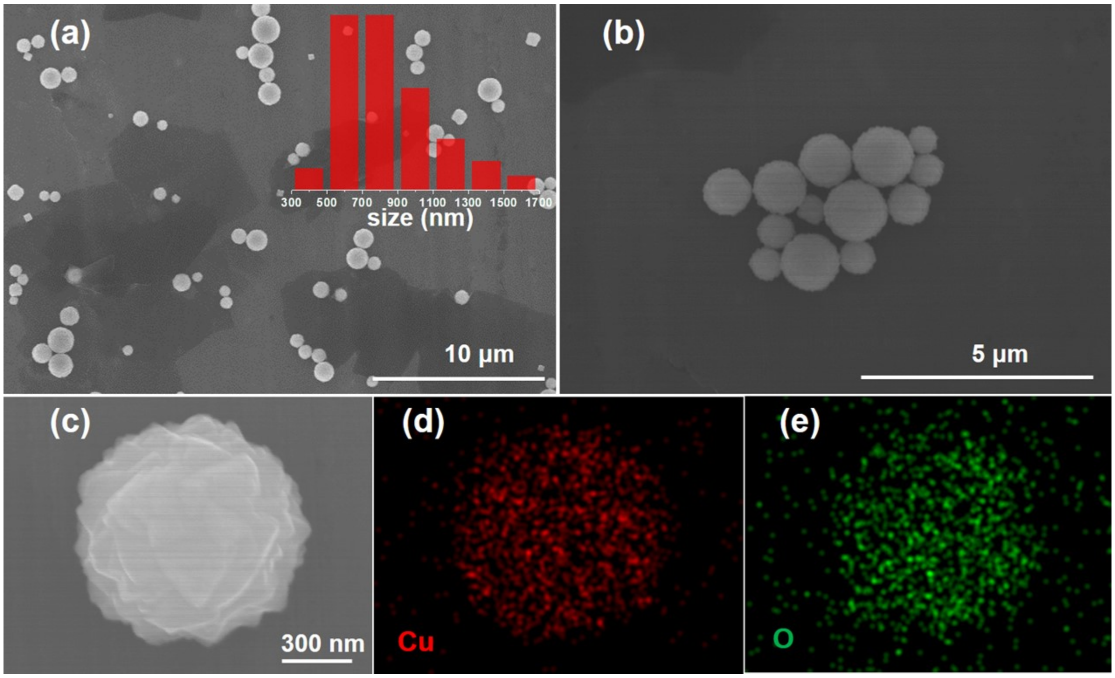

Figure S8. (a, b) SEM images of the W-CuO$_x$ sample at different magnification. Inset of (a): particle size distribution. (c) The typical SEM image of W-CuO$_x$ particle and (d, e) corresponding elemental mapping images of (d) Cu and (e) O elements, respectively.

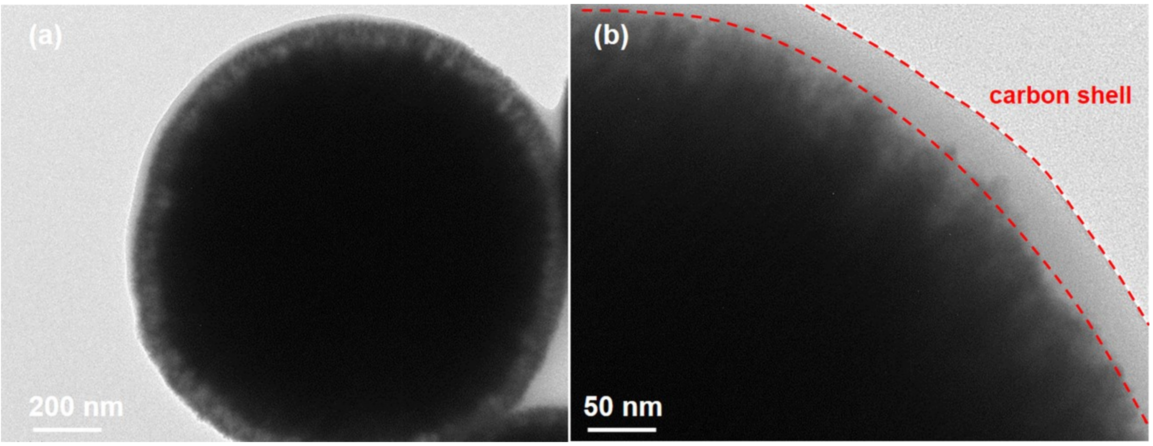

Figure S9. (a, b) TEM images of the H-CuO_x@C sample at different magnifications, exhibiting that the thickness of the carbon layer is around 50 nm.

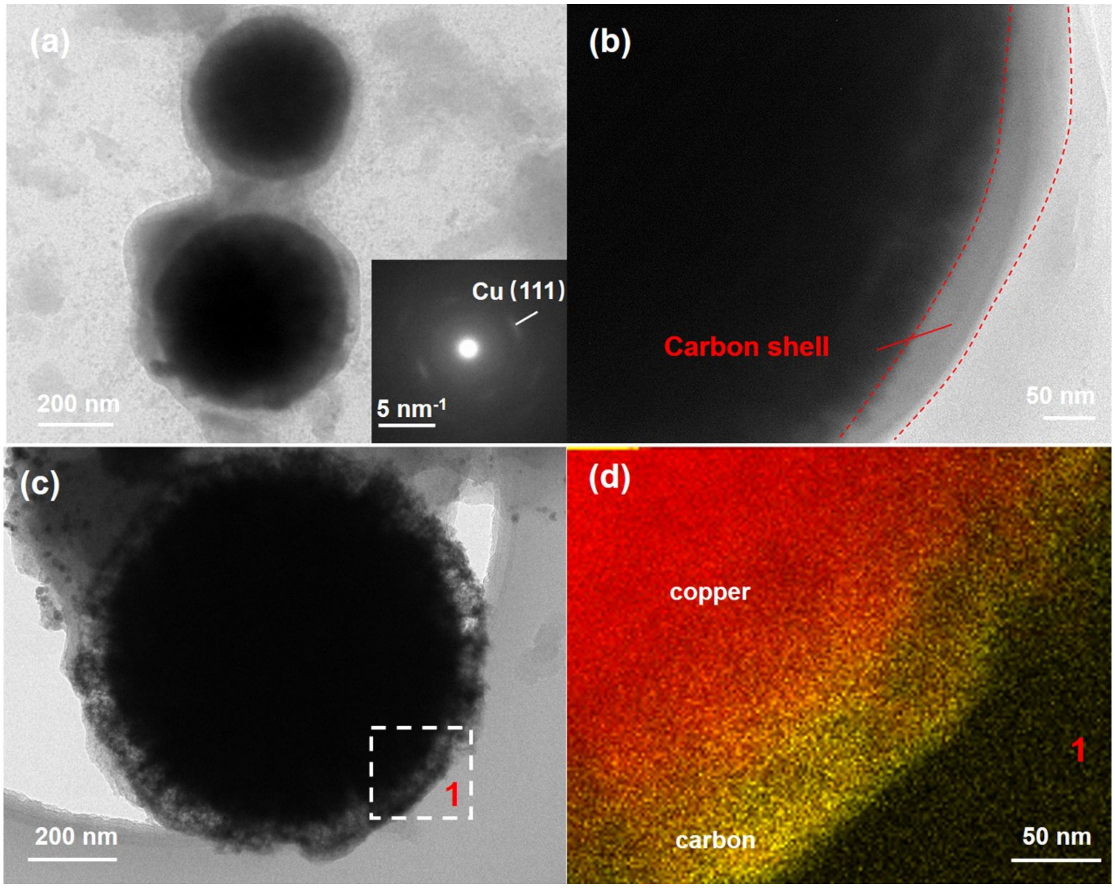

Figure S10. (a, b) TEM images of the H-CuO$_x$@C sample after 2 hours' CO$_2$RR at the applied potential of -1.40 V vs. RHE at different magnifications, indicating the tolerance of carbon shell under the electrolyte with appropriate bias. Inset of (a): the selected area electron diffraction (SAED) pattern shows that the pristine Cu$_2$O phase of H-CuO$_x$@C has been reduced to metallic Cu during the test, showing the obvious diffraction ring of Cu(111). (c) TEM image of the typical H-CuO$_x$@C particle and (d) corresponding elemental EDS mapping image of mixed Cu and C elements, showing the core-shell architecture exist during CO$_2$RR process.

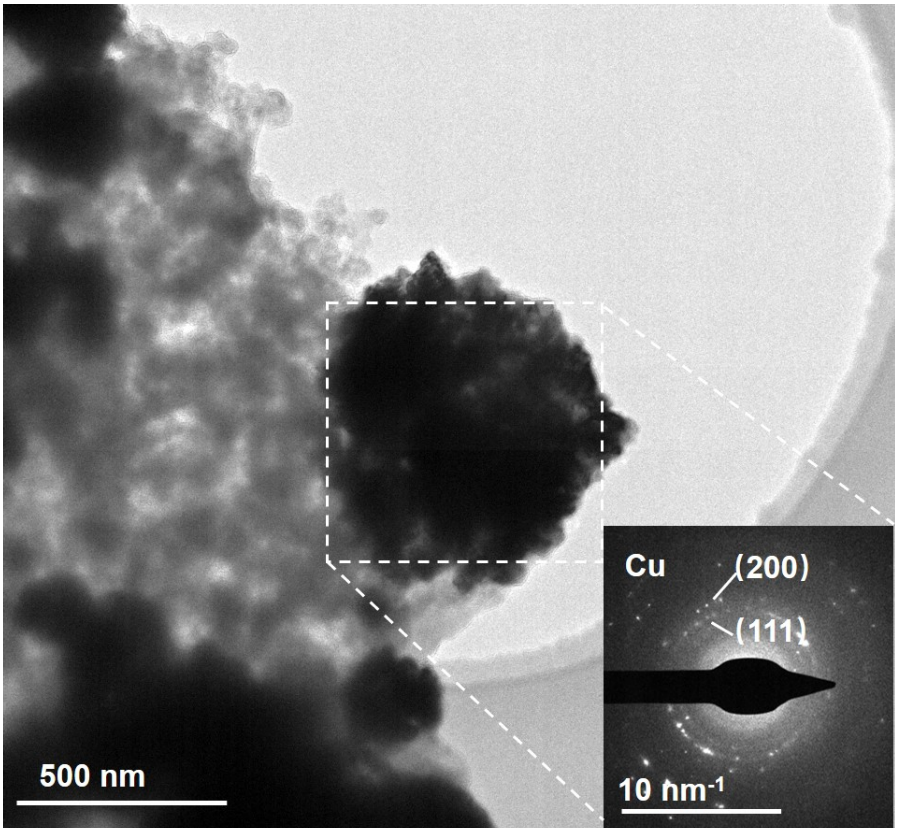

Figure S11. TEM images of the H-CuO$_x$@C sample after 2 hours' CO$_2$RR at the applied potential of -1.60 V vs. RHE, showing that the carbon shell was destroyed at the relatively high applied potential. Inset: the SAED pattern showed the Cu$_2$O phase of H-CuO$_x$@C has been reduced to metallic Cu during the test, showing the obvious diffraction ring of Cu(111).

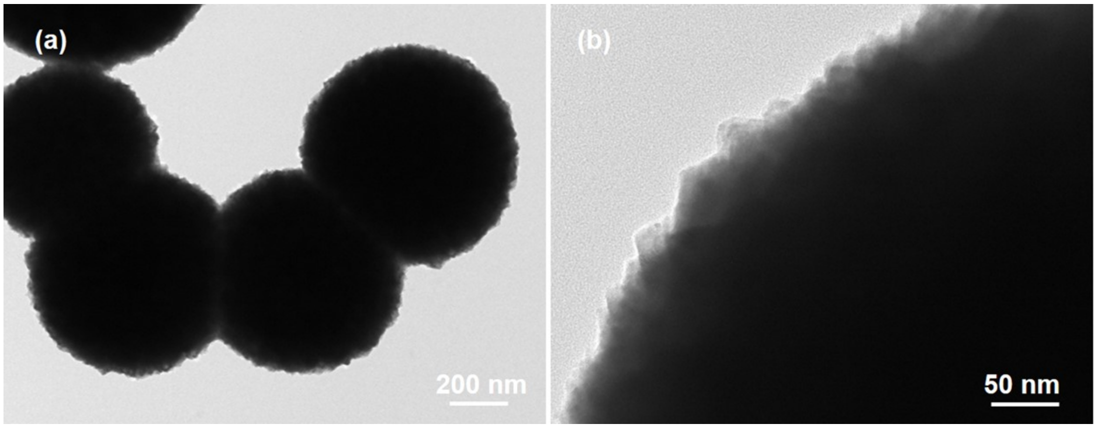

Figure S12. (a, b) TEM images of the W-CuO$_x$ sample at different magnifications, indicating no existence of the carbon shell.

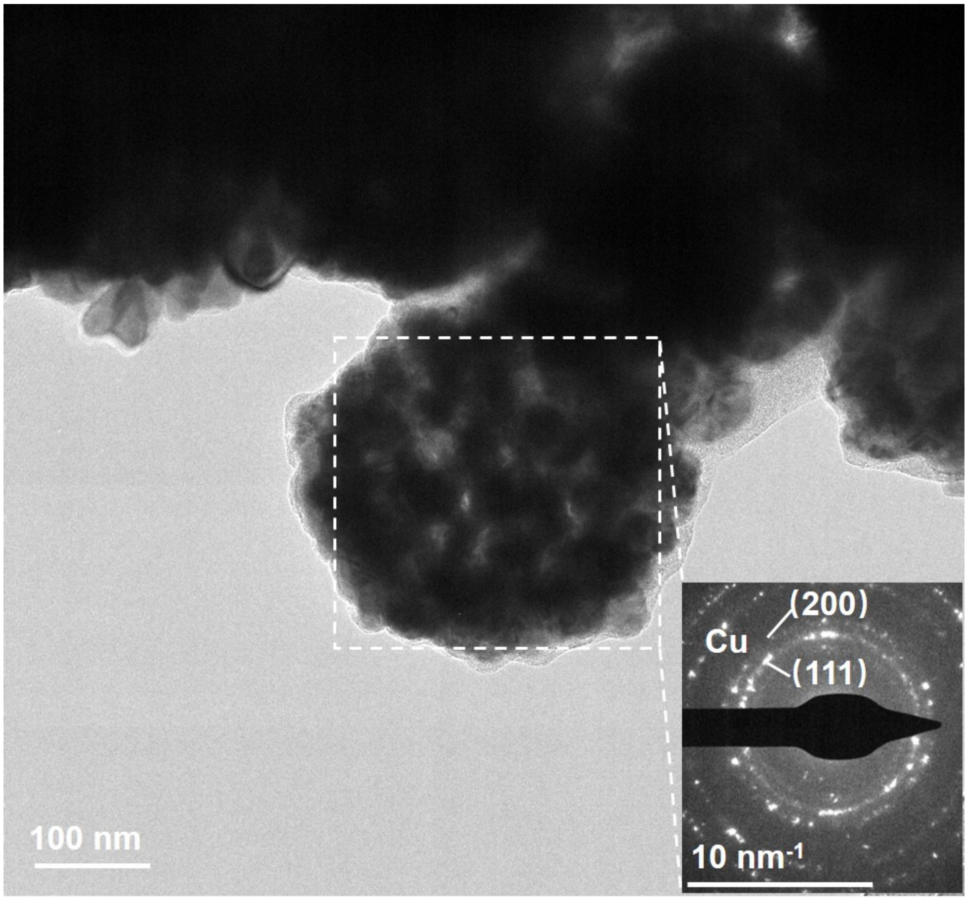

Figure S13. TEM images of the W-CuO$_x$ sample after 2 hours' CO$_2$RR at the applied potential of -1.40 V vs. RHE. Inset: the SAED pattern showed the Cu$_2$O phase of W-CuO$_x$ has been reduced to metallic Cu during the test, showing the obvious diffraction ring of Cu(111).

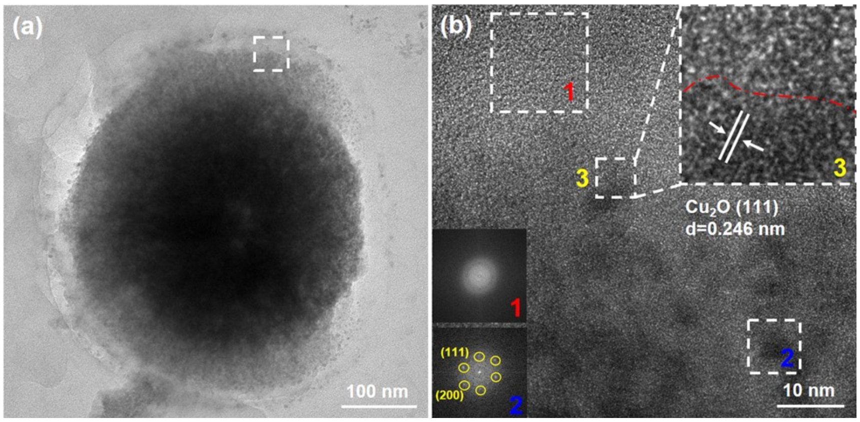

Figure S14. (a) TEM and (b) HRTEM images of the H-CuO$_x$@C ultrathin slice. Insets in the left of (b): FFT images of the square area, indicating the coexistence of the amorphous carbon shell and Cu$_2$O in the core.

Notes: A certain degree of breakage in the ultra-thin section of the sample may be caused by the section process.

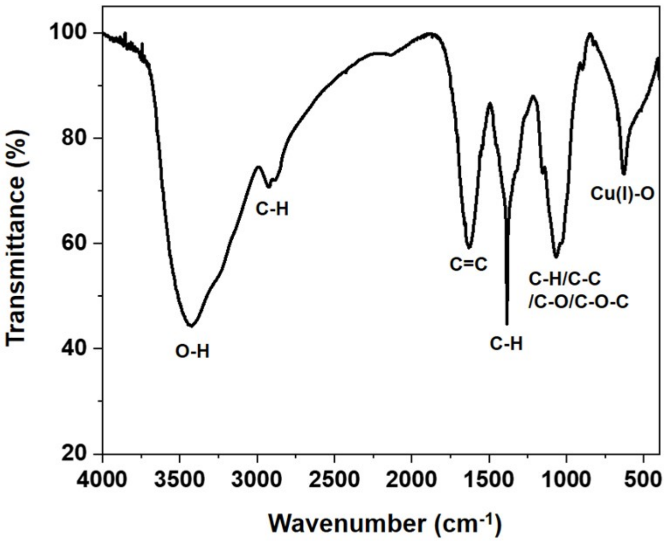

Figure S15. FT-IR spectrum of H-CuO$_x$@C, proving the existence of oxy-hydrogenated amorphous carbon and Cu$_2$O.

Notes: i) ~3400 cm^{-1}: O-H bond vibration; ii) 3000–2800 cm^{-1}: C-H symmetric and asymmetric stretching vibration from CH$_2$ and the CH$_3$ groups; iii) ~1630 cm^{-1}: olefinic group C=C stretching vibration; iv) 1380 cm^{-1}: bending vibration of C-H bond; v) 1180–910 cm^{-1}: C-H, C-C, C-O or C-O-C bond[1]; vi) 625 cm^{-1}: Cu(I)-O bond[2].

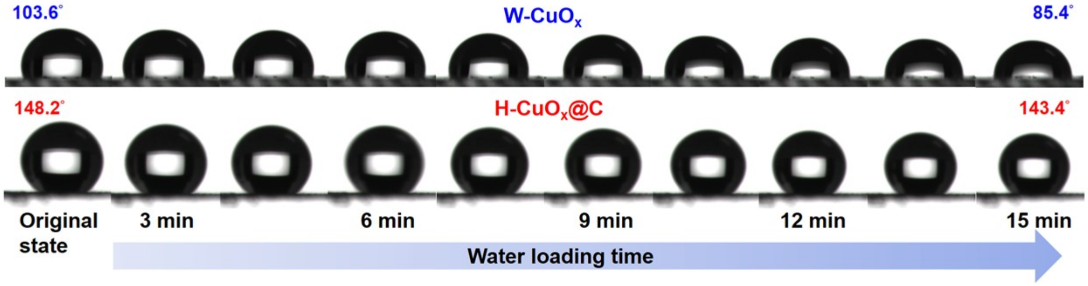

Figure S16. The time dependency of the water contact angles of W-CuO$_x$ and H-CuO$_x$@C samples, respectively, showing the durable hydrophobicity of H-CuO$_x$@C decorated electrode.

Figure S17. CA measurement of the H-CuO_x@C electrode after CO_2RR at -1.60 V for 2 h.

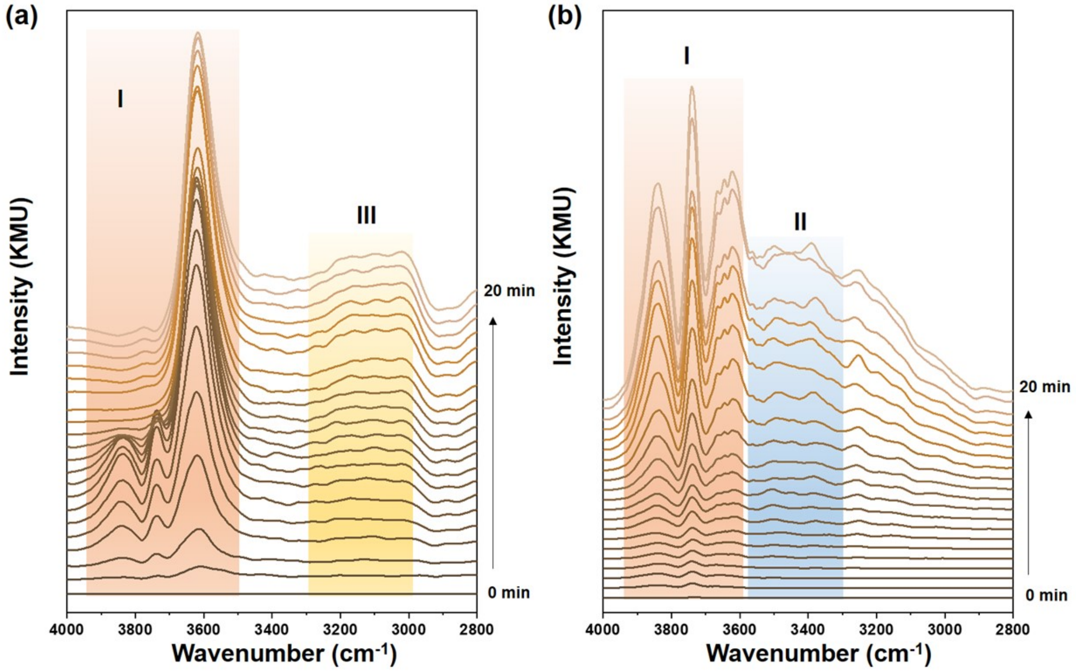

Figure S18. *In-situ* diffusion reflectance infrared Fourier transform spectra of H_2O adsorption over (a) H-CuO_x@C and (b) W-CuO_x.

Notes: Region I: free OH group[3]; Region II and III: disordered asymmetrically bonded water molecules and highly ordered water molecules, respectively[4, 5].

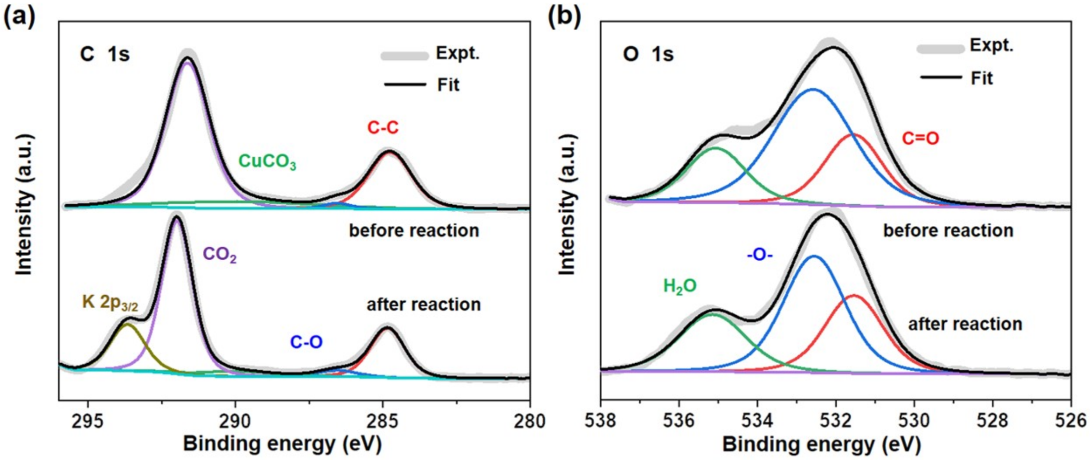

Figure S19. XPS spectra of H-CuO$_x$@C before and after 2 hours' CO$_2$RR at the applied potential of -1.40 V vs. RHE in (a) C 1s and (b) O 1s regions, indicating the CuCO$_3$ might be partially reduced. Notes: K$^+$ ions might result from the KHCO$_3$ electrolyte.

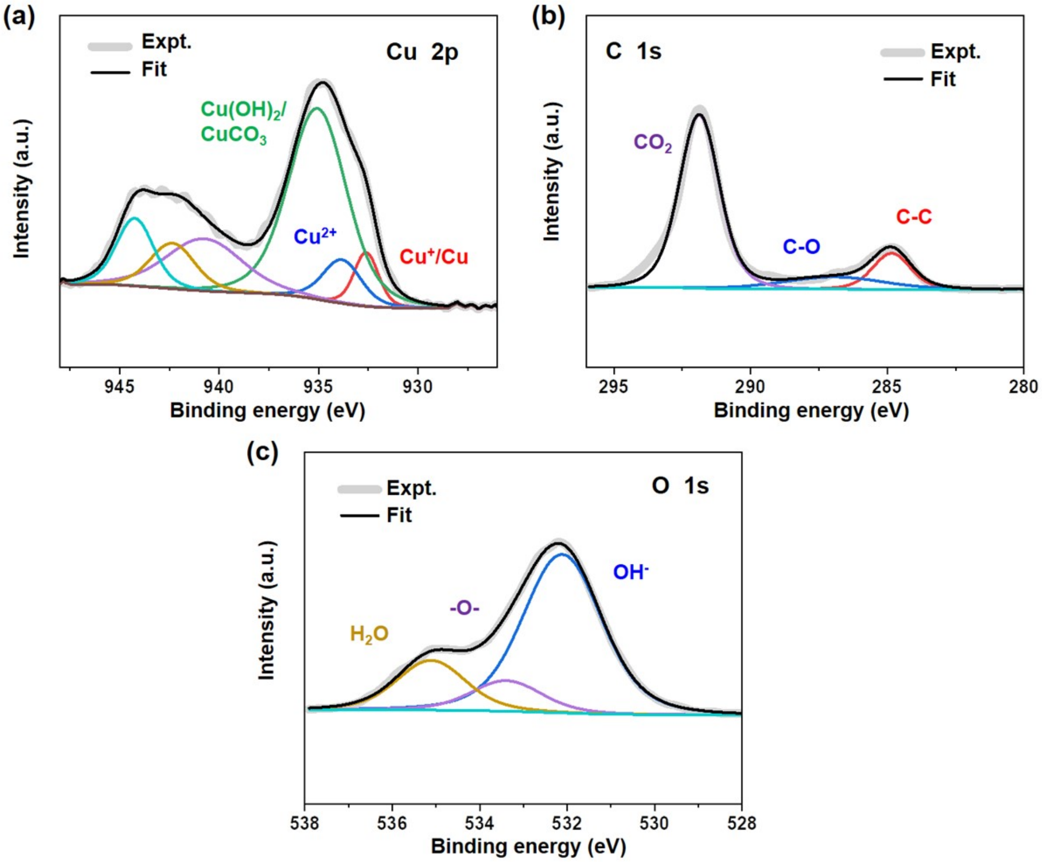

Figure S20. XPS spectra of W-CuO$_x$ in (a) Cu 2p, (b) C 1s, and (c) O 1s regions, showing that the Cu species of W-CuO$_x$ exhibit the main component of Cu^{2+}.

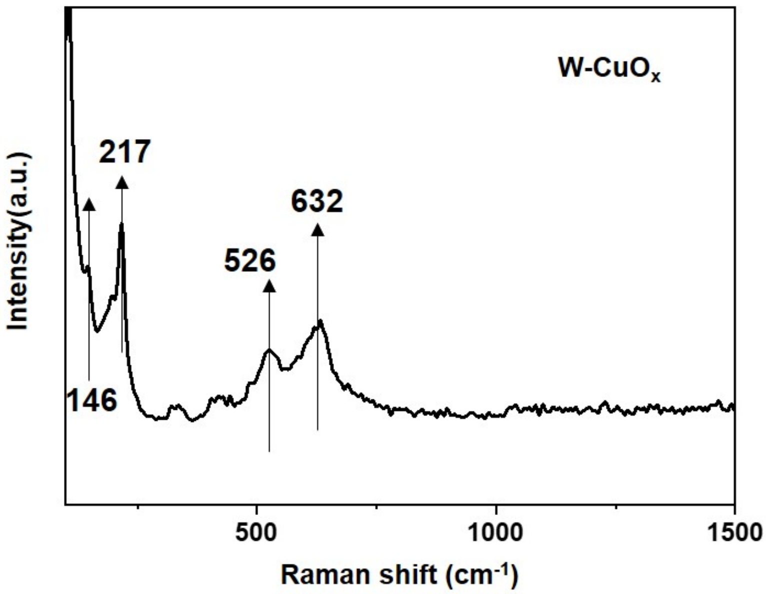

Figure S21. Raman spectrum of W-CuO$_x$, showing the existence of Cu_2O, without obvious carbon species.

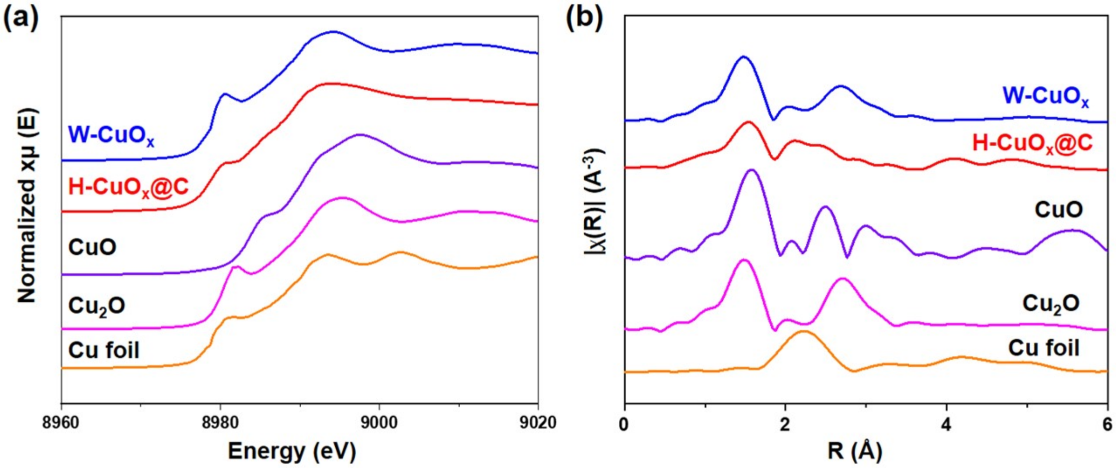

Figure S22. XAFS characterization of (a) the normalized Cu *K*-edge XANES spectra and (b) Fourier-transformed Cu *K*-edge EXAFS spectra of H-CuO$_x$@C, W-CuO$_x$, and standard materials of Cu foil, Cu$_2$O, and CuO, suggesting the reductive Cu^0 species exist in the pristine H-CuO$_x$@C sample.

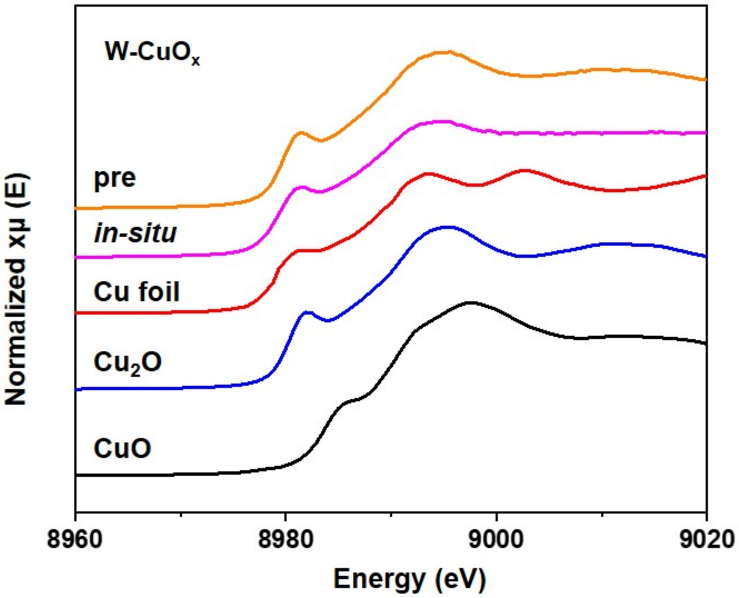

Figure S23. Normalized Cu *K*-edge operando XANES spectra of W-CuO$_x$ with standard materials of Cu foil, Cu$_2$O, and CuO, indicating the generation of metallic Cu^0 during the CO$_2$RR process.

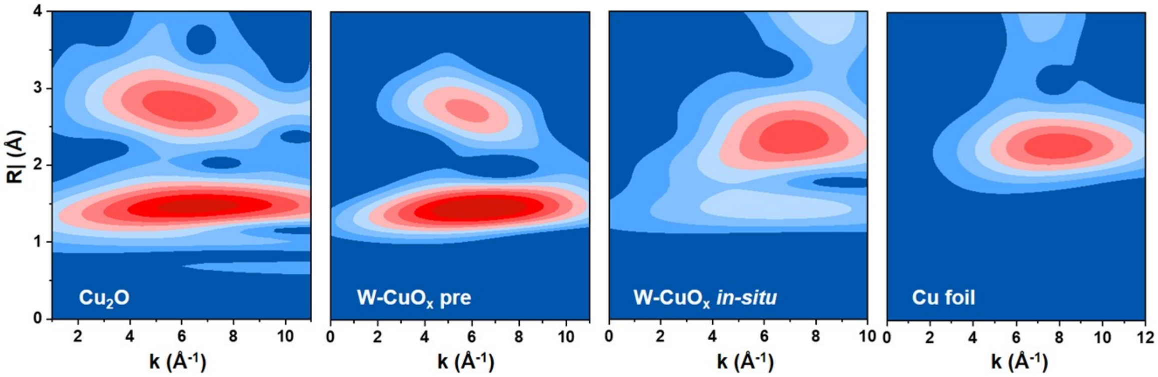

Figure S24. Morlet WT of the *k*3-weighted operando EXAFS data for the W-CuO$_x$ with standard materials of Cu foil and Cu$_2$O, suggesting the main components of metallic Cu^0 during CO$_2$RR.

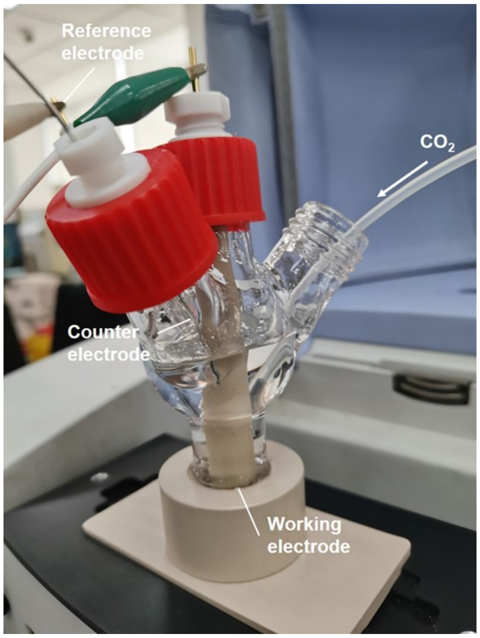

Figure S25. Digital photograph of the homemade cell attached to the PerkinElmer spectrum 100 spectrometer for ATR-IR measurement.

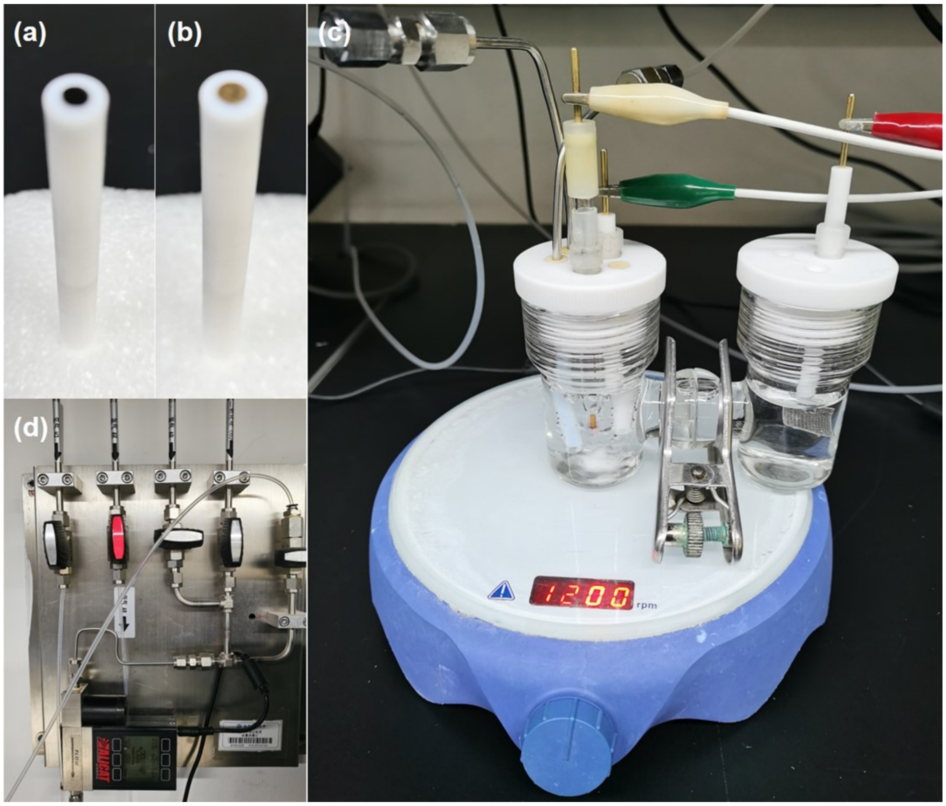

Figure S26. Digital photos of (a) glassy carbon electrode (GCE, d=3 mm) and (b) H-CuO_x@C working electrode on GCE. (c) Setup of the H-type gas-tight reactor, the stirring speed of the electrolyte was kept at 1200 r. p. m. to prevent the surface of the GCE from being covered by gas. (d) The CO_2 gas flow rate through the gas chamber was controlled as 20 sccm by a gas flow controller.

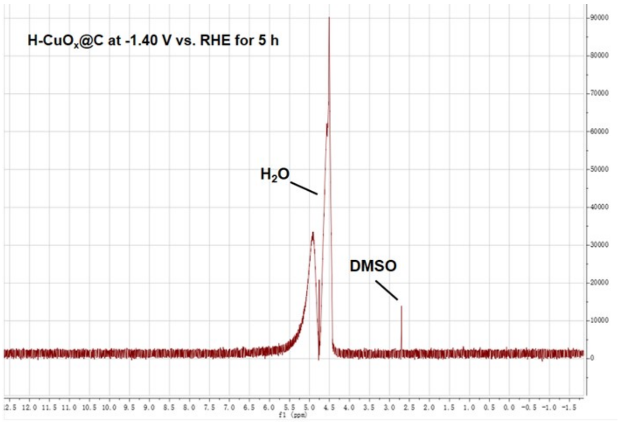

Figure S27. Typical NMR of gas product produced by H-CuO$_x$@C at the potential of -1.40 V vs. RHE for 5 h, showing no detectable liquid products.

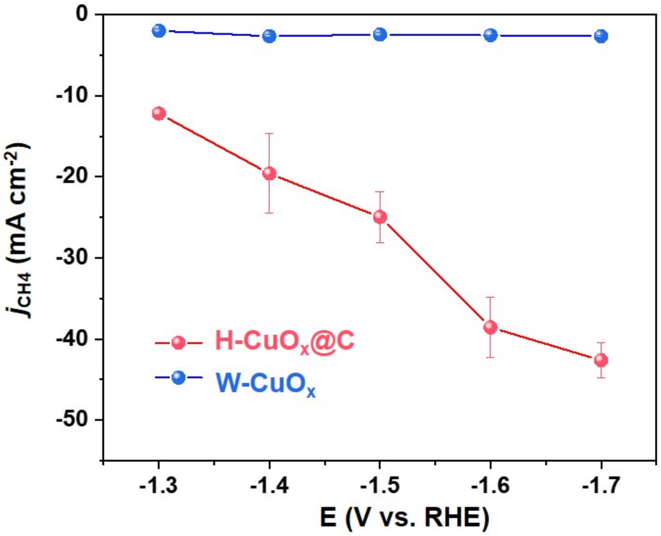

Figure S28. Potential dependence of j_{CH4} on H-CuO$_x$@C and W-CuO$_x$, exhibiting higher CH$_4$ activity for H-CuO$_x$@C.

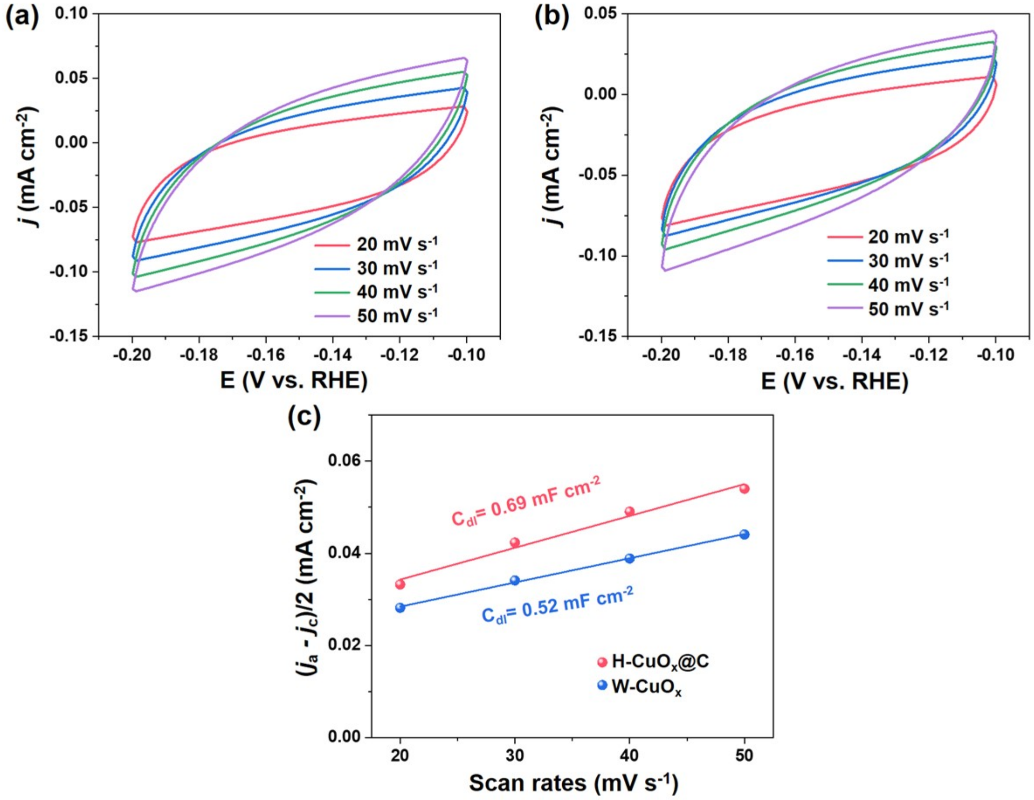

Figure S29. (a, b) CVs of (a) H-CuO$_x$@C and (b) W-CuO$_x$ collected at different scan rates, respectively. (c) The relationship between the current density and scan rate.

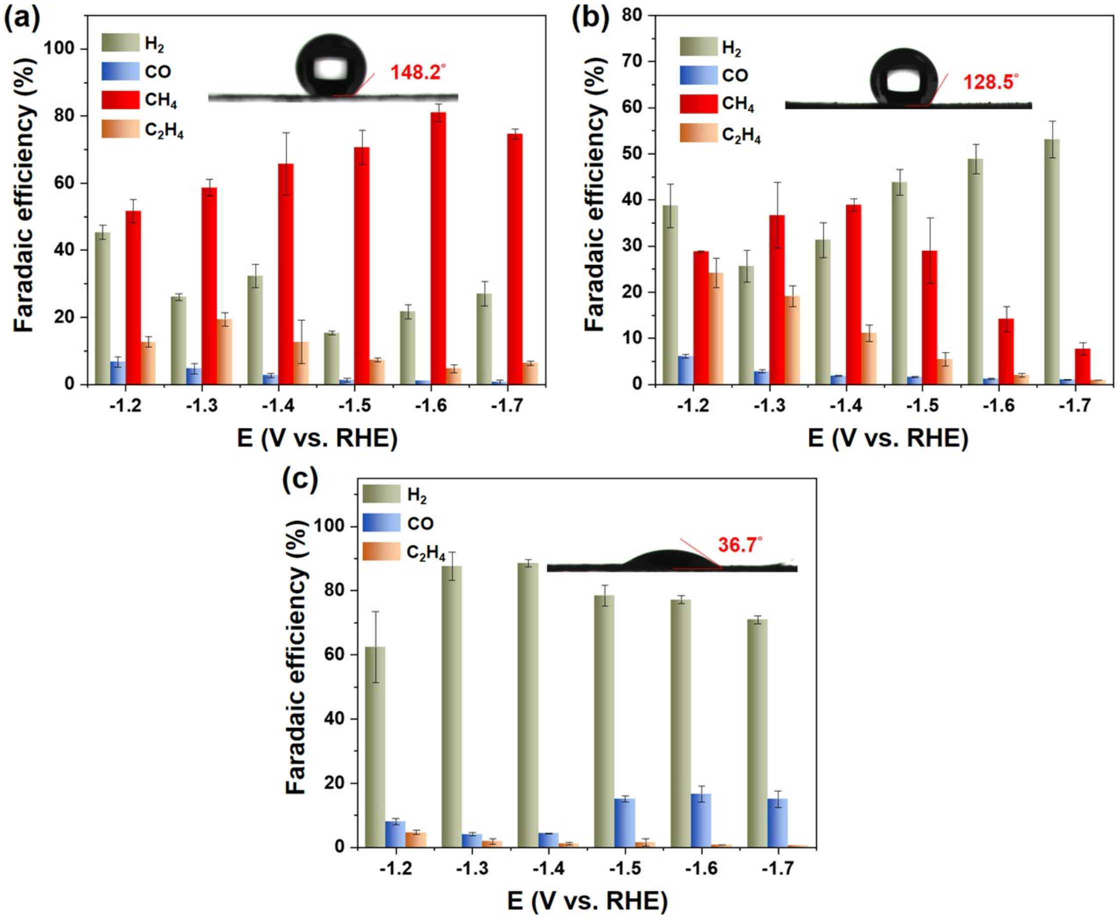

Figure S30. The faradic efficiencies of gas products on (a) H-CuO$_x$@C, (b) H-CuO$_x$@C-CTAB-1, and (c) H-CuO$_x$@C-CTAB-2. Insets: CA measurements of the (a) H-CuO$_x$@C, (b) H-CuO$_x$@C-CTAB-1, and (c) H-CuO$_x$@C-CTAB-2 electrodes.

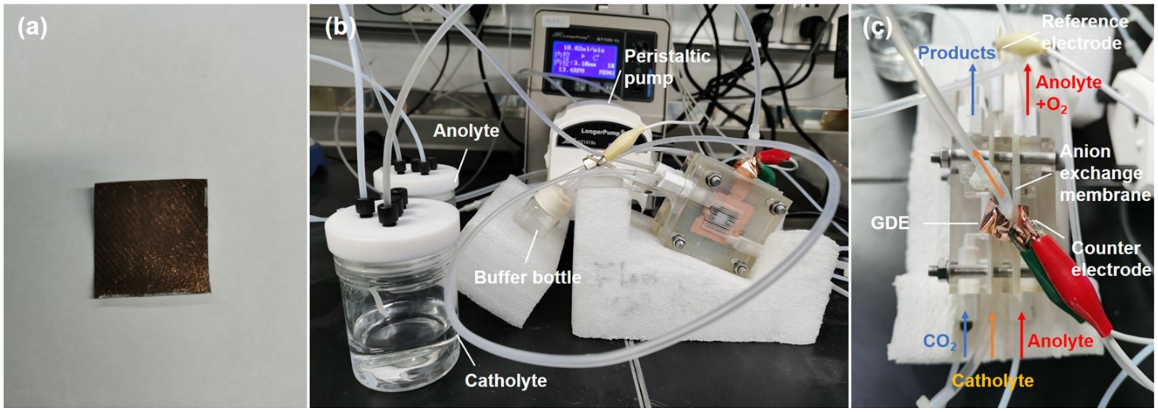

Figure S31. Digital photographs of the (a) sprayed gas diffusion electrode (GDE) with catalyst loading amount of 0.5 mg cm^{-2} and (b, c) flow cell device from (b) the side-view and (c) the top-view, respectively.

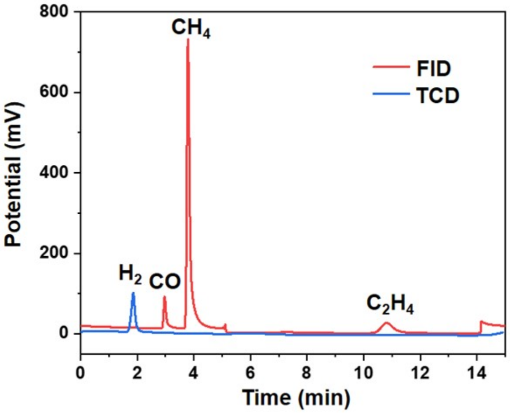

Figure S32. Typical GC of gas product produced by H-CuO$_x$@C at the current density of -500 mA cm^{-2} in 1.0 M KOH in the flow cell.

Table S1. Reaction free energies of three competing reactions (*CO desorption, protonation of *CO to*CHO/*COH, and *CO-*CO coupling) under different H_2O quantities (U = -0.74 V vs. RHE).

H_2O quantities	**Δ*G*(CO) (eV)**	**Δ*G*(*CHO) (eV)**	**Δ*G*(*COH) (eV)**	**Δ*G*(*OCCO) (eV)**
0	0.70	0.20	0.39	1.51
1	0.78	0.10	0.39	1.44
2	0.68	-0.14	0.39	1.23
3	0.74	-0.04	0.58	1.02
4	0.45	0.07	0.75	1.06
5	0.28	-0.02	0.65	0.46
…				
15	0.33	0.47	0.88	0.69

Table S2. Faradaic efficiencies of gas products for H-CuO_x@C during stability test under the current density of -700 mA cm^{-2} in 1.0 M KOH.

Time (s)	**FE_{H2} (%)**	**FE_{CO} (%)**	**FE_{CH4} (%)**	**FE_{C2H4} (%)**
5700	14.3	3.7	54.9	21.6
9300	19.0	3.5	67.6	12.9
12900	23.4	3.5	67.0	8.2
16500	25.1	3.3	65.9	6.4
19200	29.4	3.5	58.4	5.0
23700	31.4	3.7	50.1	3.6
28200	32.7	3.8	45.2	3.4

Table S3. Performance comparison between H-CuO_x@C and previously reported Cu-based electrocatalysts for CO_2-to-CH_4 conversion in the low-current density range.

Catalyst	Electrolyte	FE_{CH4} (%)	j_{CH4} (mA cm^2)	E (V vs. RHE)	Reference
H-CuO_x@C	**0.1 M $KHCO_3$**	**81**	**-39**	**-1.60**	**This work**
Cu-CD[6]	0.5 M $KHCO_3$	78	-31.2	-1.44	*Nat. Commun.*, 2021, **12**, 586.
HATNA-Cu-MOF[7]	0.1 M $KHCO_3$	78	-8.2	-1.50	*Angew. Chem. Int. Ed.*, 2021, **60**, 16409–16415.
$Cu_3(PO_4)_2$ nanosheets[8]	0.1 M $KHCO_3$	76	-15.2	-1.48	*Nano Energy*, 2021, **88**, 106239.
Cu clusters/DRC[9]	0.5 M $KHCO_3$	81.7	-18	-1.00	*Angew. Chem. Int. Ed.*, 2020, **59**, 19054–19059.
Cu Nafion[10]	0.1 M $NaHCO_3$	88	-2.5	-0.38 ^{iR}	*Energy Environ. Sci.*, 2020, **13**, 3567–3578.
$Cu_{68}Ag_{32}$[11]	0.5 M $KHCO_3$	60	-50	-1.17 ^{iR}	*J. Am. Chem. Soc.*, 2020, **142**, 12119–12132.
Cu–N–C-900[12]	0.1 M $KHCO_3$	38.6	-14.8	-1.60	*ACS Energy Lett.*, 2020, **5**, 1044–1053.
Cu twin boundaries[13]	0.2 M $KHCO_3$	59	-7.04	-1.60	*ACS Catal.*, 2020, **10**, 2026–2032.
Cu-3 mM MC[14]	0.5 M $NaHCO_3$	81.6	-31	-2.13	*J. Mater. Chem. A*, 2019, **7**, 5453–5462.
Cu(II) phthalocyanine[15]	0.5 M $KHCO_3$	66	-13	-1.06 ^{iR}	*Nat. Commun.*, 2018, **9**, 415.
Cu[16]	0.1 M $KHCO_3$	75	-10	~-1.07 ^{iR}	*ChemSusChem*, 2018, **11**, 1781–1786.
Cu-CeO_2[17]	0.1 M $KHCO_3$	58	-18	-1.80	*ACS Catal.*, 2018, **8**, 7113–7119.
Cu NWs[18]	0.1 M $KHCO_3$	55	-7.5	-1.25	*Nano Lett.*, 2017, **17**, 1312–1317.
Pd-decorated Cu[19]	0.5 M $KHCO_3$	46	-27	-0.96 ^{iR}	*Angew. Chem. Int. Ed.*, 2017, **56**, 13135–13139.
Cu-P-ED[20]	0.5 M $NaHCO_3$	85	-38	~-2.16	*ACS Catal.*, 2017, **7**, 6302–6310.
Pd@Cu RDs[21]	0.5 M $KHCO_3$	57	-17	-1.40	*ACS Nano*, 2016, **10**, 4559–4564.
Cu-porphyrin complex[22]	0.5 M $KHCO_3$	27	-13.2	-0.976 ^{iR}	*J. Am. Chem. Soc.*, 2016, **138**, 8076–8079.
n-Cu/C[23]	0.1 M $NaHCO_3$	76	-9	-1.35	*J. Am. Chem. Soc.*, 2014, **136**, 13319–13325.

Notes: ^{iR} means the potentials were *iR*-corrected.

Table S4. Performance comparison between H-CuO_x@C and previously reported Cu-based electrocatalysts for CO_2-to-CH_4 conversion in the high-current density range.

Catalyst	**Electrolyte**	**FE_{CH4} (%)**	**j_{CH4} (mA cm^2)**	**E (V vs. RHE)**	**Reference**
H-CuO_x@C	**1.0 M KOH**	**73.3**	**-366.5**	**-1.0 ^{iR}**	**This work**
		62.1	**-434**	**-1.6 ^{iR}**	
NNU-33(H)[24]	1.0 M KOH	82.17	-391	-0.9 ^{iR}	*J. Am. Chem. Soc.*, 2021, **143**, 3808–3816.
NNU-32[24]		55.1	-384	-1.0 ^{iR}	
CNP:CuPc = 4:1[25]	0.5 M $KHCO_3$	62	-136	-4.0 (cell voltage)	*Nat. Commun.*, 2021, **12**, 29324.
CoO-2.5nm/Cu/PTFE[26]	1.0 M $KHCO_3$	60	-135	-1.10 ^{iR}	*Nat. Commun.*, 2020, **11**, 6190.
Cu/PTFE[27]	1.0 M $KHCO_3$	48	-108	-1.416 ^{iR}	*J. Am. Chem. Soc.*, 2020, **142**, 3525-3531.
Cu/La_2CuO_4[28]	1.0 M KOH	56.3	-117	-1.40	*ACS Catal.*, 2020, **10**, 4640-4646.
Cu-N-5%-400[29]	1.0 M KOH	42	~-100	-1	*J. Electroanal. Chem.*, 2020, **875**, 113862.

Notes: ^{iR} means the potentials were *iR*-corrected.

REFERENCES

1 V. Ţucureanu, A. Matei and A. M. Avram, *Crit. Rev. Anal. Chem.*, 2016, **46**, 502–520.

2 A. O. Moghanlou, A. Bezaatpour, M. H. Sadr, M. Yosefi and F. Salimi, *Mat. Sci. Semicon. Proc.*, 2021, **130**, 105838.

3 J.-L. Xu and A. A. Gowen, *Spectrochim. Acta A*, 2021, **250**, 119371.

4 L. Chen, X. He, H. Liu, L. Qian and S. H. Kim, *J. Phys. Chem. C*, 2018, **122**, 11385−11391.

5 C. Lo, J. Zhang, P. Somasundaran and J. W. Lee, *J. Colloid Interf. Sci.*, 2012, **376**, 173–176.

6 Y. Cai, J. Fu, Y. Zhou, Y.-C. Chang, Q. Min, J.-J. Zhu, Y. Lin and W. Zhu, *Nat. Commun.*, 2021*,* **12***,* 586.

7 Y. Liu, S. Li, L. Dai, J. Li, J. Lv, Z. Zhu, A. Yin, P. Li and B. Wang, *Angew. Chem. Int. Ed.*, 2021*,* **60**, 16409–16415.

8 B. Zhang, J. Zhang, P. An, Z. Su, Q. Wan, X. Tan and L. Zheng, *Nano Energy.*, 2021, **88**, 106239.

9 Q. Hu, Z. Han, X. Wang, G. Li, Z. Wang, X. Huang, H. Yang, X. Ren, Q. Zhang, J. Liu and C. He, *Angew. Chem. Int. Ed.*, 2020, **59**, 19054–19059.

10 H. Pan, C. J. Barile, *Energy Environ. Sci.*, 2020*,* **13***,* 3567–3578.

11 C.-J. Chang, S.-C. Lin, H.-C. Chen, J. Wang, K. J. Zheng, Y. Zhu and H. M. Chen, *J. Am. Chem. Soc.*, 2020, **142**, 12119–12132.

12 A. Guan, Z. Chen, Y. Quan, C. Peng, Z. Wang, T.-K. Sham, C. Yang, Y. Ji, L. Qian, X. Xu and G. Zheng, *ACS Energy Lett.*, 2020, **5**, 1044–1053.

13 C. Tang, J. Shi, X. Bai, A. Hu, N. Xuan, Y. Yue, T. Ye, B. Liu, P. Li, P. Zhuang, J. Shen, Y. Liu and Z. Sun, *ACS Catal.*, 2020, **10**, 2026–2032.

14 Y. Qiu, H. Zhong, W. Xu, T. Zhang, X. Li and H. Zhang, *J. Mater. Chem. A*, 2019, **7**, 5453–5462.

15 Z. Weng, Y. Wu, M. Wang, J. Jiang, K. Yang, S. Huo, X.-F. Wang, Q. Ma, G. W. Brudvig, V. S. Batista, Y. Liang, Z. Feng and H. Wang, *Nat. Commun.*, 2018, **9**, 415.

16 K. W. Kimura, K. E. Fritz, J. Kim, J. Suntivich, H. D. Abruna and T. Hanrath, *ChemSusChem*, 2018, **11**, 1781–1786.

17 Y. Wang, Z. Chen, P. Han, Y. Du, Z. Gu, X. Xu and G. Zheng, *ACS Catal.*, 2018, **8**, 7113–7119.

18 Y. Li, F. Cui, M. B. Ross, D. Kim, Y. Sun and P. Yang, *Nano Lett.*, 2017, **17**, 1312–1317.

19 Z. Weng, X. Zhang, Y. Wu, S. Huo, J. Jiang, W. Liu, G. He, Y. Liang and H. Wang, *Angew. Chem. Int. Ed.*, 2017, **56**, 13135–13139.

20 Y. L. Qiu, H. X. Zhong, T. T. Zhang, W. B. Xu, X. F. Li and H. M. Zhang, *ACS Catal.*, 2017, **7**, 6302–6310.

21 Z. Wang, G. Yang, Z. Zhang, M. Jin and Y. Yin, *ACS Nano*, 2016, **10**, 4559–4564.

22 Z. Weng, J. Jiang, Y. Wu, Z. Wu, X. Guo, K. L. Materna, W. Liu, V. S. Batista, G. W. Brudvig and H. Wang, *J. Am. Chem. Soc.*, 2016, **138**, 8076–8079.

23 K. Manthiram, B. J. Beberwyck and A. P. Alivisatos, *J. Am. Chem. Soc.*, 2014, **136**, 13319–13325.

24 L. Zhang, X.-X. Li, Z.-L. Lang, Y. Liu, J. Liu, L. Yuan, W.-Y. Lu, Y.-S. Xia, L.-Z. Dong, D.-Q. Yuan and Y.-Q. Lan, *J. Am. Chem. Soc.*, 2021, **10**, 3808–3816.

25 Y. Xu, F. Li, A. Xu, J. P. Edwards, S.-F. Hung, C. M. Gabardo, C. P. O'Brien, S. Liu, X. Wang, Y. Li, J. Wicks, R. K. Miao, Y. Liu, J. Li, J. E. Huang, J. Abed, Y. Wang, E. H. Sargent and D. Sinton, *Nat. Commun.*, 2021, **12**, 29324.

26 Y. Li, A. Xu, Y. Lum, X. Wang, S.-F. Hung, B. Chen, Z. Wang, Y. Xu, F. Li, J. Abed, J. E. Huang, A. S. Rasouli, J. Wicks, L. K. Sagar, T. Peng, A. H. Ip, D. Sinton, H. Jiang, C. Li and E. H. Sargent, *Nat. Commun.*, 2020, **11**, 6190.

27 X. Wang, A. Xu, F. Li, S.-F. Hung, D.-H. Nam, C. M. Gabardo, Z. Wang, Y. Xu, A. Ozden, A. S. Rasouli, A. H. Ip, D. Sinton and E. H. Sargent, *J. Am. Chem. Soc.*, 2020, **142**, 3525–3531.

28 S. Chen, Y. Su, P. Deng, R. Qi, J. Zhu, J. Chen, Z. Wang, L. Zhou, X. Guo and B. Y. Xia, *ACS Catal.*, 2020, **10**, 4640–4646.

29 T. Zhang, S. Verma, S. Kim, T. T. Fister, P. J. A. Kenis and A. A. Gewirth, *J. Electroanal. Chem*., 2020, **875**, 113862.